

Contents

1 Theory	3
1.1 X-ray Diffraction Principles	3
1.1.1 Scattering at Lattices	3
1.1.2 X-rays	4
1.2 Sesquioxides	5
1.2.1 Chromium Oxide	5
1.2.2 Gallium Oxide	8
1.3 Heteroepitaxy	9
1.3.1 Pseudomorphic Growth	9
1.3.2 Relaxed Growth	11
Dislocations	11
Slip Systems for Sesquioxide Heterostructures	12
2 Experimental Methods	15
2.1 Pulsed Laser Deposition	15
2.1.1 Setup	15
2.1.2 Plasma Dynamics	17
2.1.3 Segmented Target Approach	18
2.2 X-Ray Diffraction Measurement	18
2.2.1 2θ - ω -scans	19
2.2.2 ω -scans	20
2.2.3 ϕ -scans	20
2.2.4 Reciprocal Space Maps	21
2.2.5 Technical Aspects	23
2.3 Further Methods	24
2.3.1 Thermal Evaporation	24
2.3.2 Resistivity Measurement	24
2.3.3 Thickness Determination	25
2.3.4 Spectral Transmission	26
3 Experiment, Results and Discussion	27
3.1 Preliminary Investigations	27
3.1.1 Experiment	27
3.1.2 Results	28
Oxygen Partial Pressure Variation on <i>m</i> -plane Sapphire	28
Growth Temperature Variation on <i>m</i> -plane Sapphire	32
Influence of Growth Rate on Crystal Structure	32

	Deposition on <i>c</i> -, <i>r</i> -, <i>m</i> - and <i>a</i> -plane Sapphire	34
3.1.3	Conclusion	36
3.2	Doping of Cr ₂ O ₃ Thin Films	37
3.2.1	Experiment	37
3.2.2	Results	38
	Laser Position Variation for Different Targets	38

Chapter 3

Experiment, Results and Discussion

3.1 Preliminary Investigations

In the following, the feasibility of depositing Cr_2O_3 thin films via Pulsed Laser Deposition (PLD) as well as their resulting properties are investigated. Since $\alpha\text{-Cr}_2\text{O}_3$ is the only phase of chromia (cf. 1.2.1), it is expected that the growth results in either rhombohedral or amorphous films. Furthermore, if a crystalline phase is present, the orientation with respect to the sapphire substrates is of interest. Because Al_2O_3 and Cr_2O_3 exhibit the same crystal symmetry, it is expected that the crystal orientation of the film matches the corresponding substrate orientation. Finally, deposition parameters should be optimized to obtain the best crystal quality.

3.1.1 Experiment

Due to the similar crystal structure of Cr_2O_3 and $\alpha\text{-Ga}_2\text{O}_3$, the deposition parameters of the latter were chosen as a starting point to deposit chromia thin films on $10 \times 10 \text{ mm}^2$ sapphire substrates with *m*-plane orientation. Namely, a pulse energy of 650 mJ and a pulse frequency of 20 Hz were applied for a total of 30 000 pulses. To investigate the influence of deposition parameters, three batches were produced:

1. variation of oxygen partial pressure from 8×10^{-5} to 1×10^{-2} mbar with a fixed temperature of 745°C ,
2. variation of growth temperature from 725 to 765°C with a fixed oxygen partial pressure of 1×10^{-3} mbar, and
3. variation of substrate orientation between *c*- (00.1), *r*- (01.2) *m*- (10.0) and *a*-plane (11.0) $5 \times 5 \text{ mm}^2$ sapphire substrates¹ with a fixed oxygen partial pressure of 1×10^{-3} mbar and a growth temperature of 715°C .

Structural properties of those thin films were determined by $2\theta\text{-}\omega$ -scans, ω -scans and φ -scans. The thickness was determined via spectroscopic ellipsometry, and transmission spectra were recorded for two samples of the 1st batch to determine the optical band gap. Temperature dependent resistivity measurements were performed only for the samples of the 3rd batch, because all *m*-plane oriented samples showed no conductivity at room temperature.

¹In the following, the BRAVAIS-MILLER-indices will be omitted.

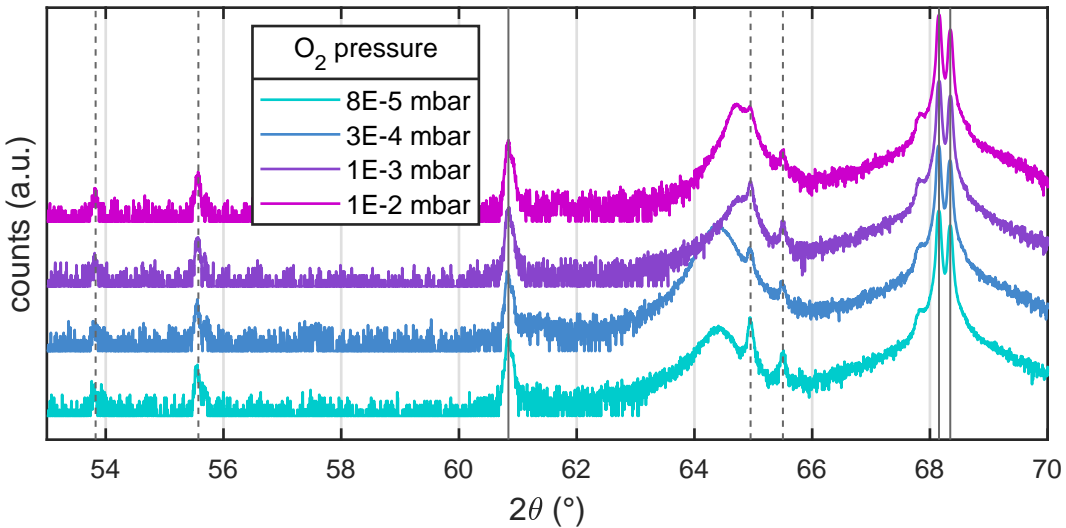


Figure 3.1: 2θ - ω -patterns of Cr_2O_3 thin films deposited on *m*-plane sapphire for various oxygen partial pressures. The solid lines indicate (30.0) substrate reflections corresponding to copper radiation, whereas the dashed lines indicate (30.0) substrate reflections corresponding to tungsten radiation.

3.1.2 Results

Oxygen Partial Pressure Variation on *m*-plane Sapphire

In the following, the results for the samples produced at four different oxygen partial pressures are analyzed. In Fig. 3.1, the 2θ - ω -patterns are depicted. For each pattern, the two peaks (solid line) at around 68° correspond to the (30.0) reflection of the *m*-plane oriented sapphire substrate. The splitting occurs due to the similar wavelength of $\text{Cu-K}\alpha_1$ and $\text{Cu-K}\alpha_2$ radiation. The additional peaks also stem mainly from the (30.0) reflection of Al_2O_3 and are caused by $\text{W-L}\beta_2$ -, $\text{W-L}\beta_1$ -, $\text{Cu-K}\beta$ -, $\text{W-L}\alpha_1$ - and $\text{W-L}\alpha_2$ -radiation (increasing angles).² In the vicinity of the calculated peak position for the (30.0) reflection of Cr_2O_3 (cf. 1.3), there is a peak observed for each sample, indicating that the α -phase of Cr_2O_3 is present. Note that the peak position is varying depending on the chosen oxygen partial pressure. The difference to the expected peak position $2\theta_0$ is expressed as out-of-plane (o.o.p.) strain ϵ_{zz} using the Bragg equation Equ. 1.9 and then

$$\epsilon_{zz} = \frac{d - d_0}{d_0} = \left(\frac{1}{\sin(2\theta/2)} - \frac{1}{\sin(2\theta_0/2)} \right) \cdot \sin(2\theta_0/2). \quad (3.1)$$

In Fig. 3.2a, the calculated strain is shown in dependence of the corresponding oxygen partial pressure. The strain decreases from approx. 0.95 % to 0.45 % with increasing pressure. This strain reduction may therefore be the result of increased background gas scattering which results in less kinetic energy of the specimen reaching the heated substrate (cf. 2.1.1).

For each sample, the 2θ angle was fixed to the observed (30.0) reflection of Cr_2O_3 and an ω -scan was performed. The Full Width at Half Maximum (FWHM) of the ω -patterns (henceforth “ ω -FWHM”) are depicted in Fig. 3.2b. The values vary between

²Klar wäre das besser das im plot an die linien zu schreiben, aber das war mir irgendwie zu auffällig es schön zu machen. Gehts auch so?

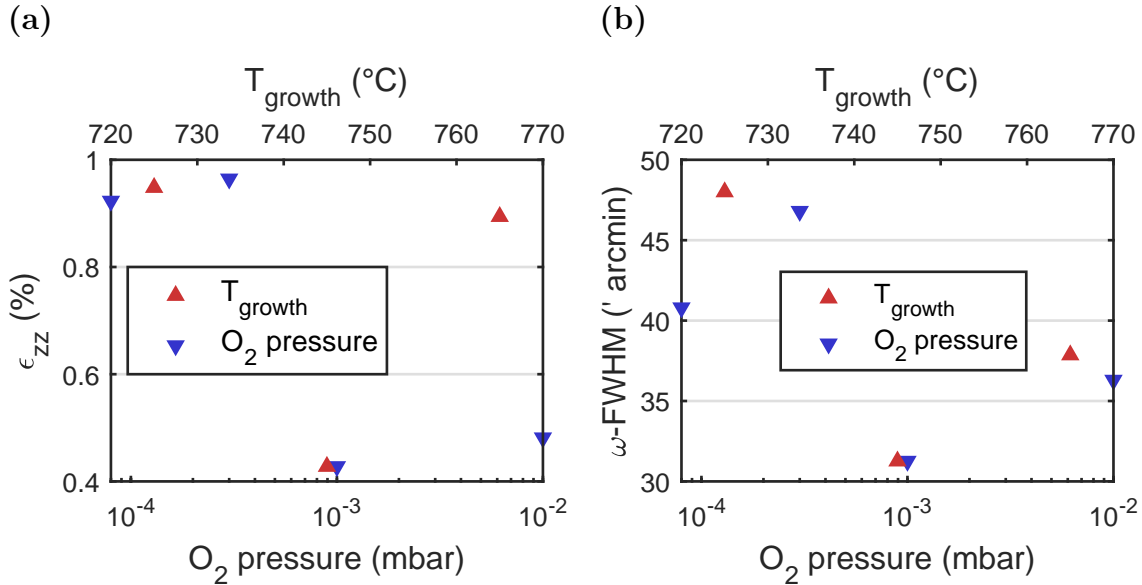


Figure 3.2: (a) o.o.p. strain calculated with Equ. 3.1 and (b) ω -FWHMs for samples from growth temperature series (red triangles, top x -axis) and oxygen partial pressure series (blue triangles, bottom x -axis).

approx. 30' and 50' and show a dependence on oxygen partial pressure, which is less pronounced compared with o.o.p. strain (Fig. 3.2a). Still, since ω -FWHM is connected to the mosaicity of the thin film, higher oxygen partial pressures yield slightly better crystal qualities. Note that due to the fact that an oxygen partial pressure of 1×10^{-3} mbar yielded the best crystal quality, this value is used for future deposition processes.

To probe for rotational domains of the thin films, φ -scans were performed by fixing 2θ and ω to the corresponding angles of the (30.6) plane of Cr_2O_3 , which has an inclination angle of 32.4° with respect to the (30.0) plane. The diffraction patterns are depicted in Fig. 3.3. The observed peaks of the thin film align with the peaks of the single crystal substrate, indicating that the film has no in-plane rotation with respect to the substrate. Furthermore, the absence of additional peaks indicates that there exists only a single domain of the thin film³.

The growth rate g varies between 3 pm pulse^{-1} and 7 pm pulse^{-1} and is depicted in Fig. 3.4a. No systematic dependence on the oxygen partial pressure can be observed.

The transmission spectra of two selected Cr_2O_3 thin films are shown in Fig. 3.5a. The samples are not fully transparent in the visible spectrum and they exhibit a greenish tint, as can also be seen in Fig. 3.4b. To determine the onset of absorption E_τ , a Tauc-plot (Fig. 3.5b) is utilized (cf. 2.3.4). The exponent is chosen to be $\frac{1}{2}$, resulting in a representation of $(\alpha E)^2$ vs. E . Although the publications used for reference in this work support the direct transition nature of Cr_2O_3 [1, 2], it has to be noted that there exist studies determining the optical band gap of Cr_2O_3 by applying an exponent of 2, assuming an indirect band gap transition for Cr_2O_3 [3, 4]. Fitting the linear regime in the onset of absorption results in $E_\tau \approx 3.7 \text{ eV}$ for both samples, which differ in strain and ω -FWHM by a factor of approx. 2 and 0.3, respectively.

³Vielelleicht müsste ich noch erwähnen warum die beiden Reflections hier bei +55° und -55° liegen, also 110° auseinander. Aber das versteh ich selber nicht so richtig :(ich

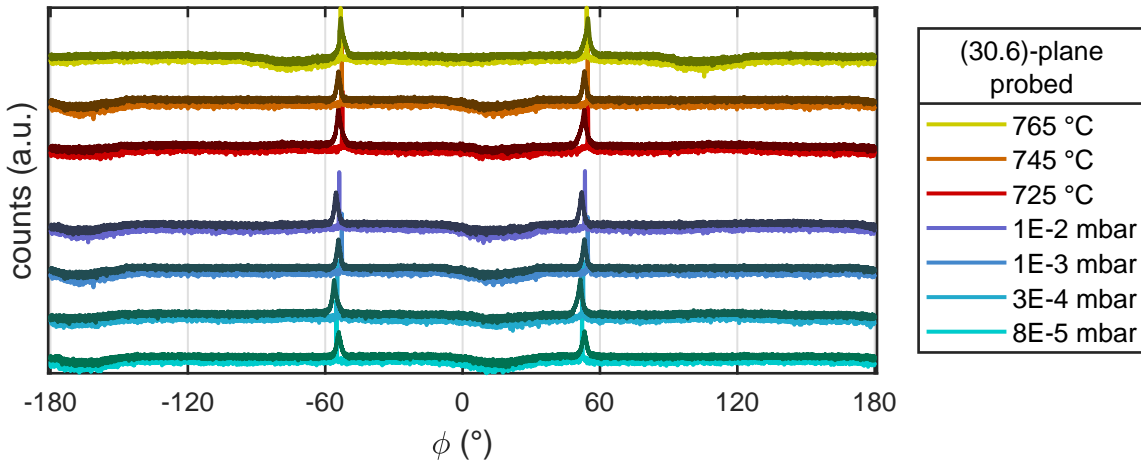


Figure 3.3: Diffraction patterns of φ -scans performed on the inclined (30.6) reflections for m -plane Cr_2O_3 (darker color) and Al_2O_3 (brighter color). The diffraction patterns cover the samples from variation of oxygen partial pressure (teal to blue colored) and variation of growth temperature (red to yellow colored).

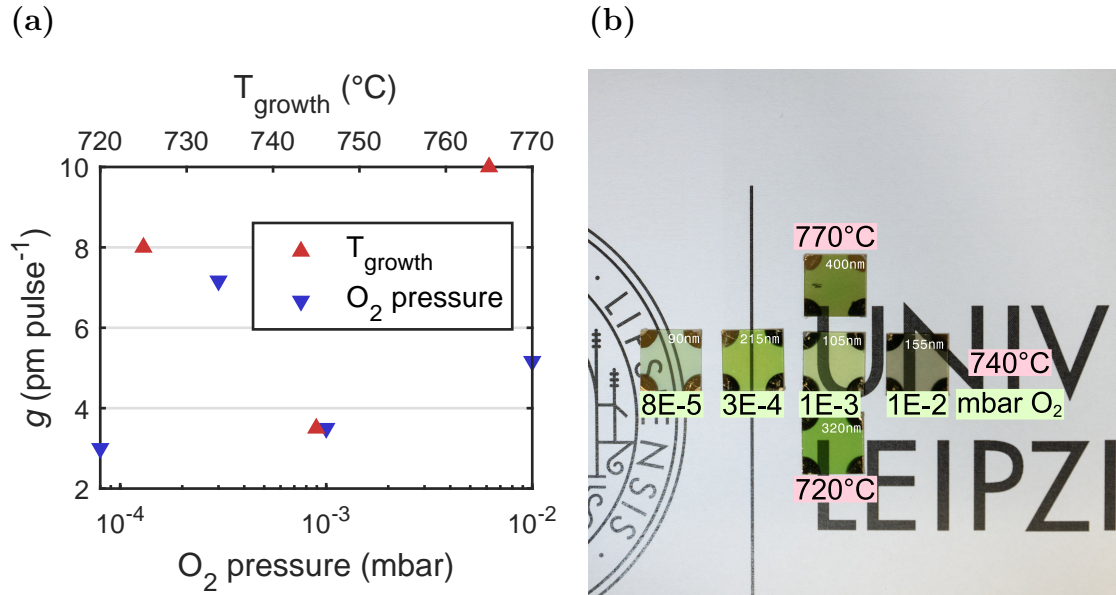


Figure 3.4: (a) Growth rates g for samples from growth temperature series (red triangles, top x -axis) and oxygen partial pressure series (blue triangles, bottom x -axis). (b) Image of the samples produced at different oxygen partial pressures and different growth temperatures.

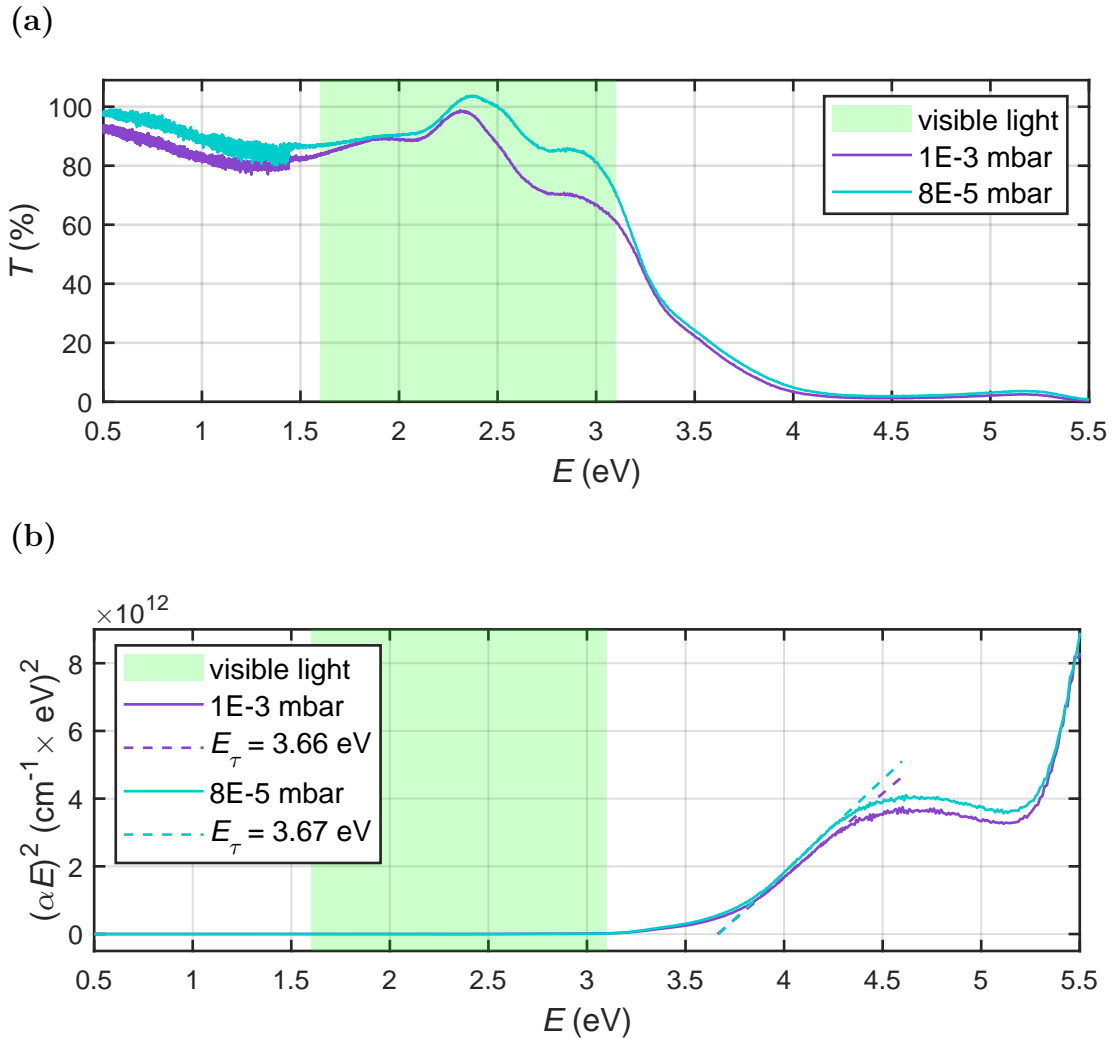


Figure 3.5: (a) Transmission spectra of two selected Cr_2O_3 thin films, deposited with different oxygen partial pressures. The spectra are normalized to a corresponding uncoated m -plane sapphire substrate. (b) Tauc-plot of the above-mentioned samples. It is assumed that Cr_2O_3 has a direct bandgap [1, 2].

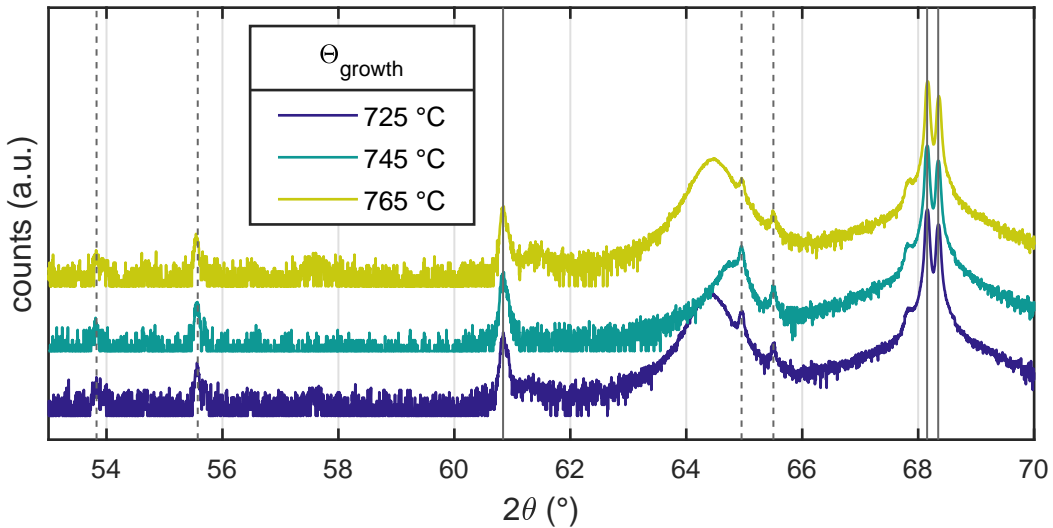


Figure 3.6: 2θ - ω -pattern of Cr_2O_3 thin films deposited on *m*-plane sapphire for three different growth temperatures. The lines indicate substrate reflections that stem from copper and tungsten radiation (cf. 3.1)

Growth Temperature Variation on *m*-plane Sapphire

In the following, the results for the three samples produced at different growth temperatures are presented. Similar to the previous results, the (30.0) reflection of the α -phase of Cr_2O_3 can be observed (Fig. 3.6). Note that the additional peaks are corresponding to the (30.0) reflection of the substrate and stem from various radiation wavelengths. The calculated o.o.p. strain is shown in Fig. 3.2a and a large spread of strain can be observed, varying between 0.4 % and 1 %. Note that there is no systematic dependence on growth temperature. The ω -FWHMs of the Cr_2O_3 (30.0) reflection are shown in Fig. 3.2b and exhibit a similar spread as the samples with varying oxygen partial pressure, but similar to the o.o.p. strain, no dependence on growth temperature is observed. The φ -scans (Fig. 3.3) show that the thin films are in-plane aligned with the respective substrate and that no rotational domains are present. Finally, the growth rate varies between $3.5 \text{ pm pulse}^{-1}$ and 10 pm pulse^{-1} with no observable dependence on growth temperature.

Influence of Growth Rate on Crystal Structure

It has to be noted that there is a large spread in strain and ω -FWHM for the samples that were deposited at different growth temperatures. The range of temperature variation was only $40 \text{ } ^{\circ}\text{C}$ and has no significant influence on the distribution of strain and ω -FWHM (Fig. 3.2). Because all the other process parameters were kept the same⁴, this indicates that another parameter influences the crystal quality. This is supported by the fact that the growth rate correlates with the magnitude of strain and ω -FWHM, as can be seen in Fig. 3.7a. Although strain is related to ω -FWHM, it has to be noted that for a small regime of o.o.p. strain around approx. 0.9 %, the ω -FWHM scatters

würde erwarten dass sie 180° auseinander liegen.

⁴In fact, for the last two samples produced ($\Theta = 725 \text{ } ^{\circ}\text{C}$ and $\Theta = 765 \text{ } ^{\circ}\text{C}$), the pulse number was increased to 40 000 pulses. This was due to the fact that the growthrate decreased.

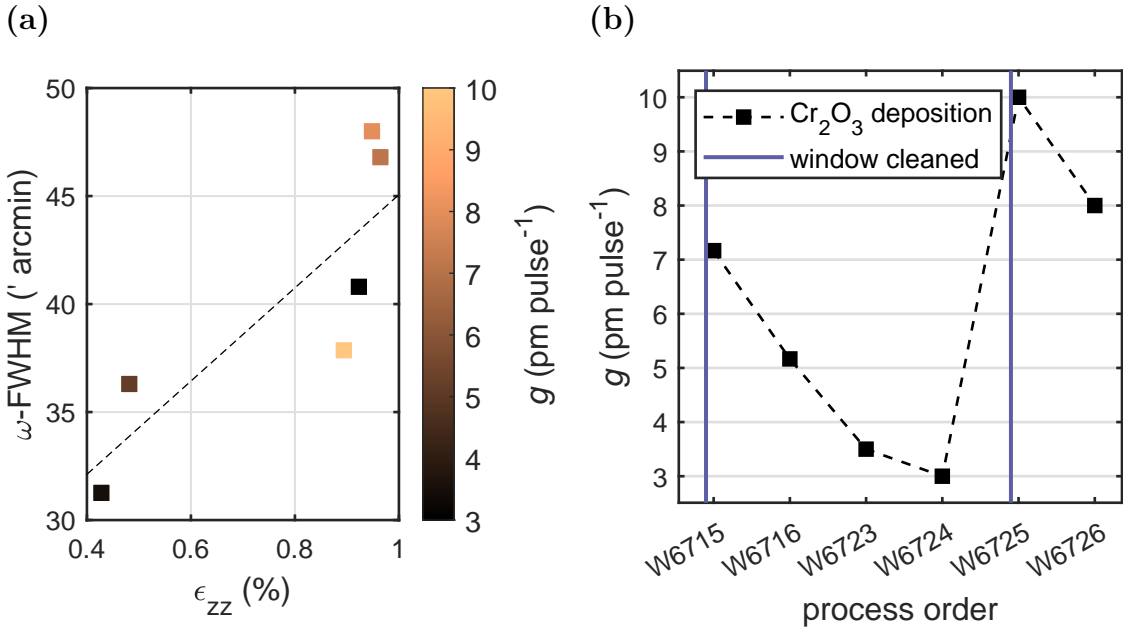


Figure 3.7: (a) Correlation of ω -FWHM with o.o.p. strain, as well as correlation of both with growth rate g (false color). The dashed line is a linear fit serving as guide to the eye. (b)

between approx. $37'$ and $47'$.

The origin of the varying growth rate – and therefore varying crystal quality – can be found when taking the number of processes into account that were performed before. In Fig. 3.7b, the growth rate is visualized depending on the order of sample fabrication. It is also indicated when the laser entrance window has been cleaned. It is common practice to clean the latter every couple of processes due to coating with target material which absorbs laser energy. But from Fig. 3.7b it becomes clear that this should be done much more frequently when working with Cr_2O_3 . Note that the laser has a wavelength of 248 nm, corresponding to 5.0 eV, which is not transmitted by Cr_2O_3 thin films⁵, as can be seen in Fig. 3.5a. Therefore, the increasing coating of the laser entrance window with each new process absorbs a large amount of laser pulse energy, resulting in less fluence on the PLD target. This results in less ablated target material and less kinetic energy of the ablated species, which leads to a reduced growth rate and different crystal growth conditions that have higher strain and ω -FWHM as a result.

This explanation is supported by the dependence of crystal quality on oxygen partial pressure (cf. Fig. 3.2). There, the increment of crystal quality with higher oxygen pressures is attributed to the increased background gas scattering resulting in less kinetic energy of the plasma material. This also explains the outlier in Fig. 3.7a, where one sample corresponds to a higher strain and ω -FWHM of approx. 0.9% and $41'$, respectively (black square). This is not expected when considering the rather small growth rate of 3 pm pulse^{-1} (W6724 in Fig. 3.7b). But when taking account for the fact that this sample is fabricated at a very low oxygen partial pressure of 8×10^{-5} mbar,

⁵To be precise, the transmission spectrum in Fig. 3.5a is recorded for *m*-plane oriented *crystalline* Cr_2O_3 thin films. This may not be the present phase when Cr_2O_3 deposits on the (colder) window made out of glass, where it may form an amorphous phase.

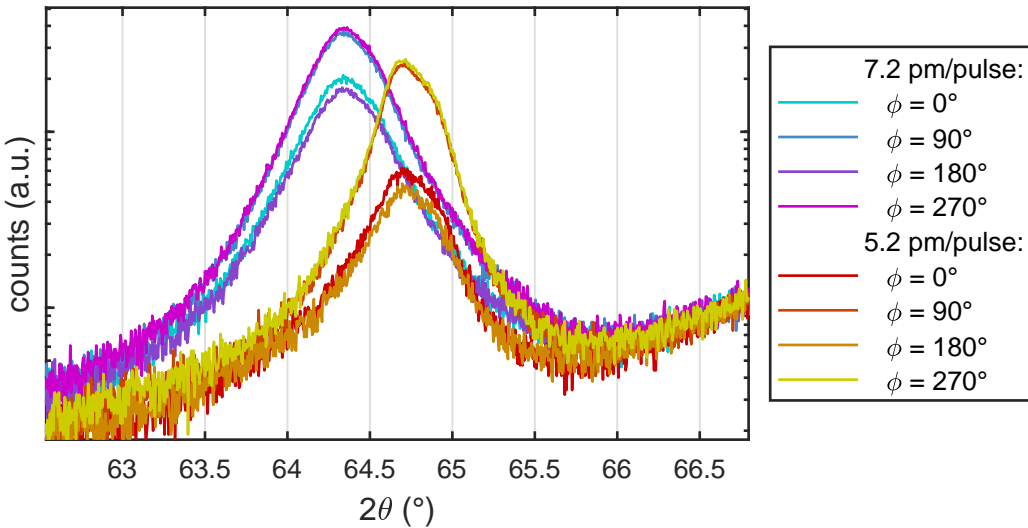


Figure 3.8: 2θ - ω -patterns for two samples in four different azimuths each.

it becomes clear that although the reduced fluence on the target would generally lower the kinetic energy of the plasma material, the limited scattering with the background gas counteracts this effect, resulting in the observed crystal quality.

It is noteworthy that the observed strain (cf. Fig. 3.2a) is distributed around two distinct values of approx. 0.4 % and 0.9 %. A prior reported thin film tilt for *m*-plane oriented rhombohedral heterostructures [5] may be the reason for this observation: the samples are installed in the XRD device in such a way that the *c*-axis is either parallel or orthogonal to the scattering plane. This orientation is arbitrary, and thus the (expected) thin film tilt is either along the X-ray beam or perpendicular to it, which could result in unexpected results when calculating the o.o.p. lattice plane distance from the observed peak position. To check if this is the origin of the observed strain, for two samples of different strain according to Fig. 3.2, four 2θ - ω -scans were performed with incrementing the azimuth by 90° after each measurement. The resulting diffraction patterns are depicted in Fig. 3.8. The strain is independent of azimuth, only the peak intensity is altered by the in-plane rotation of the sample. For both samples, an azimuth of 0° and 180° results in a lower intensity, supporting the hypothesis that the (expected) thin film tilt is perpendicular to scattering plane which results in a deviation from the BRAGG condition. Therefore, the distribution of observed strain is not a measurement artifact.

Deposition on *c*-, *r*-, *m*- and *a*-plane Sapphire

For the samples deposited on substrates with different orientation, 2θ - ω -patterns were recorded (Fig. 3.9). For each sample, the expected substrate peaks are observed: (00.6) and (00.12) for *c*-plane; (01.2), (02.4), (03.6) and (04.8) for *r*-plane; (30.0) for *m*-plane; (11.0) and (22.0) for *a*-plane. Several smaller peaks also correspond to those reflections but stem from other X-rays than Cu-K α (cf. Fig. 3.1). The mentioned reflections are also observed for the Cr₂O₃ thin film, but with a shift in 2θ position similar to the previously investigated *m*-plane samples (Tab. 3.1). Note that for *r*-plane, the higher order reflections of Cr₂O₃ cannot be observed. It can be concluded that Cr₂O₃ grows

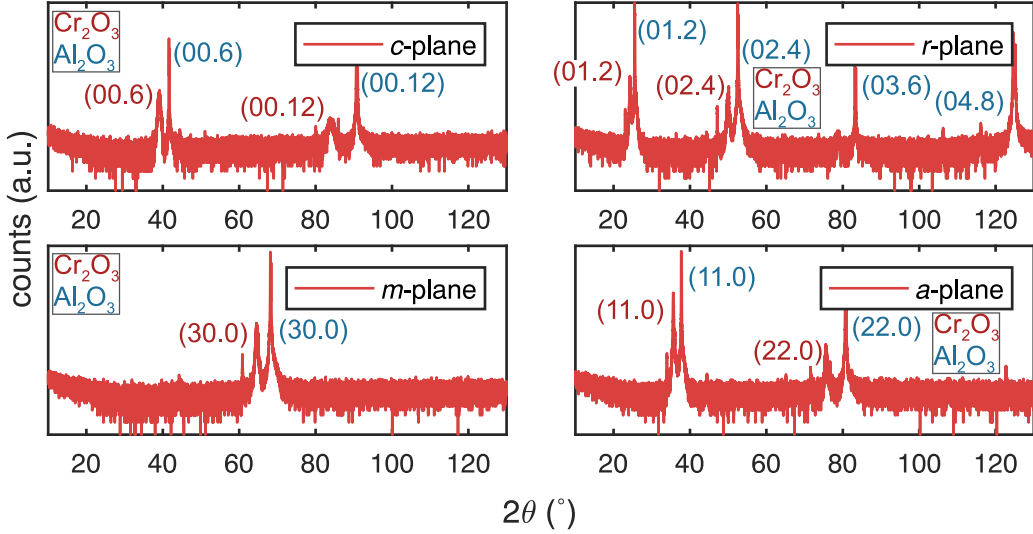


Figure 3.9: 2θ - ω -patterns of Cr_2O_3 thin films deposited on *c*-, *r*-, *m*- and *a*-plane sapphire.

Table 3.1: Structural parameters, approximate resistivity at room temperature and activation energy for Cr_2O_3 thin films of different orientation.

Plane	ϵ_{zz} (%)	ω -FWHM (')	ρ (Ωcm)	E_A (meV)
<i>c</i>	1.71	42.6	3	57, 34
<i>r</i>	0.72	38.4	120	117
<i>m</i>	0.55	42.6	3600	240
<i>a</i>	1.41	32.4	4900	259

in the α -phase on sapphire substrates of different orientation, where the thin film orientation matches the corresponding substrate. Henceforth, “*c*-plane Cr_2O_3 ” will refer to a Cr_2O_3 thin film deposited on *c*-plane oriented $5 \times 5 \text{ mm}^2$ sapphire substrates, and so on. For each sample, ω -scans were performed on the (00.6), (02.4), (30.0) and (11.0) reflections for *c*-, *r*-, *m*- and *a*-plane, respectively. The resulting ω -FWHMs are in the range of approx. $30'$ to $40'$ (Tab. 3.1).

Because the resistivity of all samples was too high to measure Hall effect, only resistivity measurements (cf. 2.3.2) were performed for several temperatures (Fig. 3.10). The resistivity depends strongly on the orientation of the thin film, the resistivities at room temperature are listed in Tab. 3.1. A difference of more than three orders of magnitude between *c*-plane and *a*-plane samples is observed. The linear behavior of the ARRHENIUS-plot⁶ indicates a thermally activated mechanism for conductivity, and thus semiconductive behavior. Note that no further conclusions can be drawn on the conduction mechanisms due to the missing carrier concentration and mobility data. By assuming a behavior of the form

$$\rho \propto \exp\left(\frac{E_A}{k_B T}\right), \quad (3.2)$$

with BOLTZMANN constant k_B , an activation energy E_A can be estimated. Those

⁶Visualization of $f(T)$ as $f'(\tau)$ with $f' = \log f$ and $\tau = 1/T$.

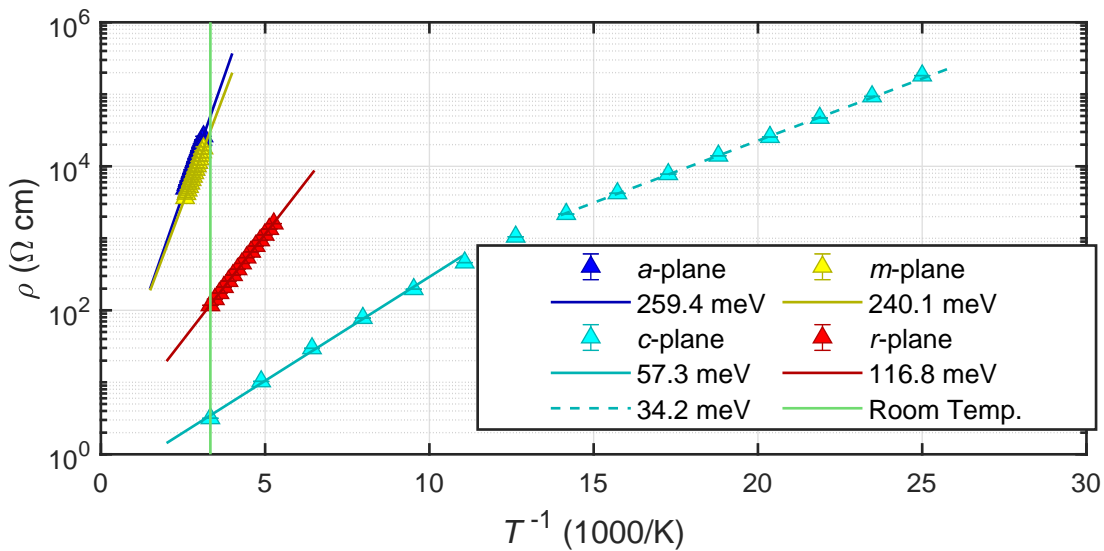


Figure 3.10: Temperature dependent resistivity measurements for samples with different orientations.

energies are also listed in Tab. 3.1. For *c*-plane Cr₂O₃, two linear regimes can be distinguished, favoring a dependence of the form

$$\rho \propto a \exp\left(\frac{E_{A,1}}{k_B T}\right) + b \exp\left(\frac{E_{A,2}}{k_B T}\right), \quad (3.3)$$

thus two activation energies are determined.

3.1.3 Conclusion

m-plane Cr₂O₃ thin films can be deposited over a wide range of oxygen partial pressure of more than 2 orders of magnitude. It turned out that the main influence on the crystal quality correlates with the growth rate and is due to a variation of the laser pulse fluence on the target. Nevertheless, an oxygen partial pressure of 1×10^{-3} mbar and a growth temperature of 750 °C are chosen for deposition of subsequent thin films. α -Cr₂O₃ could also be deposited on *c*-, *r*- and *a*-plane sapphire, with the thin films crystallizing in the respective orientation. Note that all deposited thin films showed a discrepancy between observed o.o.p. lattice plane distance and values predicted from Tab. 1.1. The conductivity is strongly dependent on the crystal orientation and was very low for the prismatic orientations, but with 0.3 S cm^{-1} three orders of magnitude higher for the basal orientation.

3.2 Doping of Cr_2O_3 Thin Films

The resistivity of the Cr_2O_3 thin films showed strong dependence on thin film orientation. To improve and taylor the conductivity, it is tried to incorporate acceptors into the *p*-type material. The elements chosen for this are Cu and Zn, because doping has already been accomplished on *c*-plane sapphire with magnesium via MgO [1]. Furthermore, it is tried to improve the ohmic behavior of the contacts of the thin films.

3.2.1 Experiment

To fabricate doped thin films, three different PLD targets were applied. Each target was eliptically segmented (cf. 2.1.1), with the outer region consisting of pure Cr_2O_3 . The inner region (ellipse) was also Cr_2O_3 but with a fraction of dopant, namely:

1. 0.01 wt.% CuO, called “CuO-doped”,
2. 0.01 wt.% ZnO, called “ZnO-doped (low)” and
3. 1 wt.% ZnO, called “ZnO-doped (high)”.

For each target, several processes were done with the laser spot position varying on the target. For each process, deposition was done on all of the 4 aforementioned substrate orientations to check whether the conductivity of the prismatic orientations could be improved. The composition of the ablated material can be calculated via Equ. 2.1, but this does not account for the finite area illuminated by the laser pulse. A simple model for including this effect can be achieved by simulating N several randomly distributed points r_i in the range Δr around a radial laser position r_{PLD} . Then, the composition x_D can be calculated as the mean of the N calculated compositions for each r_i . The resulting dependence of x_D on r_{PLD} is visualized in Fig. 3.11, where a higher value of Δr results in more smeared out graphs. A target with inner concentration of 0.01 wt.% dopant was assumed (Cu-doped target or Zn-doped (low) target). The Monto Carlo simulations can further be approximated by a linear fit, which was done for $\Delta r = 2 \text{ mm}$ (blue dotted line in Fig. 3.11). Henceforth, the different samples fabricated with different radial laser spot positions r_{PLD} are characterized by the expected composition x_D calculated from this linear fit. The reason for this is that according to Equ. 2.1, when applying r_{PLD} smaller than the length of the semi-minor axis of the inner ellipse, no variation in composition would be observed, even though the real finite laser spot size results in a different result.

To improve the contacts for resistivity measurements, samples were produced using the ZnO-doped (low) target and a fixed $r_{\text{PLD}} = 3 \text{ mm}$. Only *c*- and *r*-plane sapphire substrates were used and the deposition temperature was varied between 560°C and 680°C . For each growth temperature, subsequent contacting was done with Ti-Al-Au for a *c*-plane and an *r*-plane sample, as well as Ti-Au for a *c*-plane and an *r*-plane sample. Furthermore, the *c*-plane samples contacted with Ti-Al-Au were compared before and after annealing at 210°C in nitrogen atmosphere.

2ϑ - ω -scans were performed for every sample, but ω -scans for *c*- and *r*-plane samples only. The thickness was determined using spectroscopic ellipsometry. Resistivity measurements at room temperature were done using the PAUW method, which was

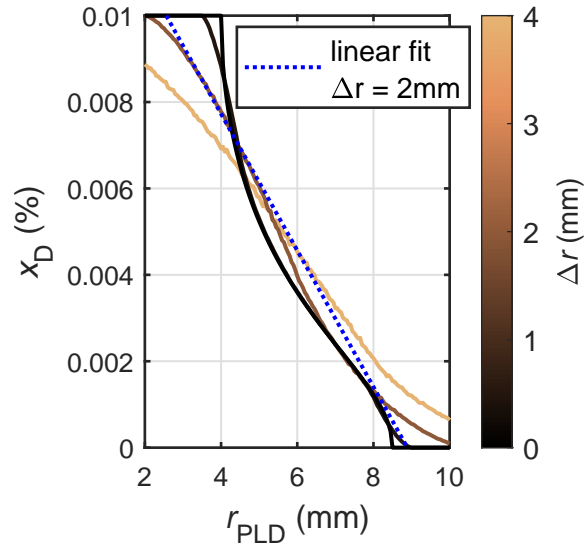


Figure 3.11: Predictions for the plasma plume composition x_D using Monte Carlo simulations with $N = 10\,000$ and different values for Δr .

also applied when conducting temperature dependent resistivity measurements on one *c*-plane sample of each target. Note that the effect of infrequent cleaning of the laser entrance window that was described in 3.1 was discovered during the execution of those experiments, which is why the samples produced from the ZnO-doped (high) target were the only ones for which this effect could be prevented.

3.2.2 Results

Laser Position Variation for Different Targets

Bibliography

- [1] L. Farrell et al. “Conducting mechanism in the epitaxial *p*-type transparent conducting oxide Cr₂O₃:Mg”. In: *Physical Review B* 91.12 (2015), p. 125202. ISSN: 1098-0121, 1550-235X. DOI: [10.1103/PhysRevB.91.125202](https://doi.org/10.1103/PhysRevB.91.125202).
- [2] Zhishan Mi et al. “The effects of strain and vacancy defects on the electronic structure of Cr₂O₃”. In: *Computational Materials Science* 144 (2018), pp. 64–69. ISSN: 09270256. DOI: [10.1016/j.commatsci.2017.12.012](https://doi.org/10.1016/j.commatsci.2017.12.012).
- [3] Chun-Shen Cheng, H. Gomi, and H. Sakata. “Electrical and Optical Properties of Cr₂O₃ Films Prepared by Chemical Vapour Deposition”. In: *Physica Status Solidi (a)* 155.2 (1996), pp. 417–425. ISSN: 00318965, 1521396X. DOI: [10.1002/pssa.2211550215](https://doi.org/10.1002/pssa.2211550215).
- [4] M.F. Al-Kuhaili and S.M.A. Durrani. “Optical properties of chromium oxide thin films deposited by electron-beam evaporation”. In: *Optical Materials* 29.6 (2007), pp. 709–713. ISSN: 09253467. DOI: [10.1016/j.optmat.2005.11.020](https://doi.org/10.1016/j.optmat.2005.11.020).
- [5] Max Kneiß et al. “Strain states and relaxation for α -(Al_xGa_{1-x})₂O₃ thin films on prismatic planes of α -Al₂O₃ in the full composition range: Fundamental difference of a- and m-epitaxial planes in the manifestation of shear strain and lattice tilt”. In: *Journal of Materials Research* 36.23 (2021), pp. 4816–4831. ISSN: 0884-2914, 2044-5326. DOI: [10.1557/s43578-021-00375-3](https://doi.org/10.1557/s43578-021-00375-3).